Microstructural effects on the spall failure of 7085 aluminum alloy

Dung-Yi Wu[a,1], Chengyun Miao[b,1], Christopher S. DiMarco[b], Debjoy D. Mallick[b,d], K.T. Ramesh[a,b,c], Todd C. Hufnagel[a,b,c]

[a] *Department of Materials Science and Engineering, Johns Hopkins University, Baltimore, MD, 21218, USA*
[b] *Hopkins Extreme Materials Institute, Johns Hopkins University, Baltimore, MD, 21218, USA*
[c] *Department of Mechanical Engineering, Johns Hopkins University, Baltimore, MD, 21218, USA*
[d] *US Army DEVCOM Army Research Laboratory, 321 Colleran Road, Aberdeen Proving Ground, MD 21005-5066, USA*

Abstract

Designing aluminum alloys for spall resistance requires an understanding of the active failure mechanisms under dynamic loading. However, it is time-consuming and expensive to obtain sufficient data to investigate these mechanisms from conventional plate impact spall experiments. Here we use a high-throughput laser-driven micro-flyer plate impact technique to connect the spall failure of aluminum alloy Al7085-T711 to its microstructure. By conducting tests at four impact velocities, we observe the full range of behaviors from incipient spall to complete spall failure. The spall strength of Al7085-T711 increases with both increasing strain rate and peak shock stress, as is typically the case in aluminum alloys. Examination of recovered samples indicates that incipient spall voids initiate primarily at Al_7Cu_2Fe second-phase particles. To further explore the effect of microstructure on spall failure, we annealed some specimens at 500 °C to increase the aluminum grain size while retaining the Al_7Cu_2Fe particles, which had only a minor effect on spall strength. Solutionizing at 600 °C to eliminate the Al_7Cu_2Fe second-phase particles, on the other hand, increases the spall strength significantly. Our results suggest that spall failure of Al7085-T711 is dominated by the presence Al_7Cu_2Fe second-phase particles, and that eliminating these particles could result in improved spall resistance of commercial alloys.

Email addresses: ramesh@jhu.edu (K.T. Ramesh), hufnagel@jhu.edu (Todd C. Hufnagel)
[1] Both authors contributed equally to this work.

Keywords: Spall failure mechanism, Laser shock, Microstructure effects, Aluminum alloys, Heat treatment.

---

1. Introduction

Spall failure is a shock-induced failure mechanism in which shock wave interactions from high-velocity impact generate intense hydrostatic tensile stresses; these stresses cause void nucleation, growth, and coalescence [**?** **?**] in metals. The spall behavior of aluminum alloys is critical for withstanding extreme conditions, and has been extensively studied [**?** **?** **?** **?** **?** **?** **?** **?**]. Spall failure is a process that is affected by the applied conditions (such as tensile strain rate and the stresses associated with the prior compressive shock) as well as the microstructure (which may evolve as a result of the compressive shock). For example, Williams and coworkers found that the spall strength of 1100 aluminum increases with peak shock stress for both fully annealed and cold-rolled material [**?** **?**]. On the other hand, Stevens and coworkers found that the spall strength of 6061-T6 aluminum was not significantly influenced by the peak shock stress [**?**]. These apparently contradictory results indicate that the microstructure is an important factor determining spall behavior.

The role of microstructure in spall is complicated by the complexity of the failure process itself, which includes stages of void nucleation, growth, and coalescence. Microstructure can influence spall behavior directly, for example by providing nucleation sites for voids, and through its effect on dynamic strength, which affects the rate of void growth. Initiation of spall failure occurs by nucleation of voids at microstructural features such as second-phase particles or grain boundaries [**?** **?**]. The growth of these voids requires plastic deformation of the material, and the plasticity is influenced by factors such as dislocation mobility, solid-solution strengthening, precipitate strengthening, and grain size. As an example of this complexity, grain size can influence spall in terms of both nucleation and growth, so that a variety of behaviors are possible. Brewer and coworkers found that a recrystallized Al-3Mg alloy had a lower spall strength than high-purity aluminum with larger grain size, a reduction they attributed to reduced propensity for ductile transgranular fracture at the smaller grain sizes [**?**]. Chen and coworkers observed that the spall strength of aluminum was only affected by the grain size at low shock stresses, and the spall strength became independent of grain size at higher shock stresses [**?**]. Pedrazas and

coworkers also found no influence of grain size on the spall strength, but did observe a transition to ductile transgranular fracture above a critical grain size [**?**].

Traditional spall tests use a gas gun to propel a flyer plate towards a target plate of the material at high velocity. In this technique, the samples are large (mm–cm scale) compared to the characteristic length scales of the microstructure (microns). As a result, the measured response in a single test is an average over the microstructural distribution. In contrast, the recently-developed laser-driven micro-flyer (LDMF) plate impact technique [**?** **?** **?** **?**] uses samples with much smaller volumes, and thus the results are likely to be more sensitive to microstructural variations over scales larger than the samples. At the same time, the relatively low cost of these LDMF tests makes it feasible to probe the statistics of this variability by conducting a large number of tests.

In this work, we describe the use of the laser-driven micro-flyer technique together with photon Doppler velocimetry (PDV) to study the spall response of a commercial 7085 aluminum alloy, both in a commercial temper (T711) and after heat treatment to increase the aluminum grain size and eliminate the Al_7Cu_2Fe second-phase particles. We examine the effects of the shock loading parameters and microstructure (grain structure and second-phase particles) on spall failure. The as-received Al 7085-T711 specimens were impacted at velocities of $630\,\mathrm{m\,s^{-1}}$ to $1140\,\mathrm{m\,s^{-1}}$, resulting in different strain rates and shock stresses. Post-spall samples were characterized using x-ray computed tomography (CT) and scanning electron microscopy (SEM) to develop a microstructure-based understanding of the active spall failure mechanisms.

2. Experimental methods

2.1. Sample preparation and microstructural characterization

We purchased a one-inch (25.4 mm) thick plate of 7085-T711 rolled aluminum alloy from Arconic (Pittsburgh, USA). The T711 temper denotes that the material was slightly over-aged, giving it higher yield strength and improved ballistic performance comparing to aluminum alloy 7085 without heat treatment [**?**]. In addition to testing material in this condition (which we refer to as the "as-received" state), we

manipulated the microstructure by heat treating some specimens in air followed by a quench into room-temperature water. After heat treatment, the specimens were stored at $-20\,^{\circ}\mathrm{C}$ to minimize aging prior to testing.

X-ray diffraction (XRD) was performed on a Bruker D8 Focus diffractometer with a LynxEye detector using Cu-Kα radiation. Scanning electron microscopy (SEM) was performed with a Tescan Mira 3 GM SEM at a beam voltage of 20 keV. Energy-dispersive spectroscopy (EDS) and electron-backscatter diffraction (EBSD) data were collected with a beam voltage of 25 keV. Following the spall tests the internal spall voids were characterized by x-ray micro computed tomography (micro-CT) using an RX Solutions EasyTom micro-CT at 50 kV and a nominal voxel size of 1.5 µm.

2.2. Quasi-static constitutive behavior and wave speed measurement

In order to gauge the effect of annealing on constitutive behavior, we performed room temperature tensile tests at a strain rate of $1.25 \times 10^{-3}\,\mathrm{s}^{-1}$ using an MTS Criterion Series 40 electromechanical test system equipped with a 5 kN load cell. Strain in the gauge section was measured using a customized digital image correlation (DIC) system. We used electro-discharge machining (EDM) to prepare flat dog-bone tensile samples with a gauge length of 8 mm, width of 2 mm, and thickness of 0.8 mm. Three tests were conducted for each condition to ensure reproducibility.

2.3. Measurement of elastic wave speeds and moduli

Reduction of the spall data requires knowledge of the wave speeds of the test material. We measured the elastic wave speeds of as-received 7085-T711 in the through-thickness (plate normal) direction using a laser ultrasonic technique [**?**]. The wave speed data along with the measured density were then also used to compute the elastic properties of the material (Table 1).

2.4. Laser-driven micro-flyer spall testing

We used a laser-driven micro-flyer technique to conduct spall tests [**?** **?**]. The laser used here is a Quanta–Ray PRO–350 Nd:YAG pulsed laser, with 10 Hz pulse frequency and ∼10 ns pulse duration. The wavelength is 1064 nm, and the maximum

Table 1: Elastic wave speeds and material properties of as-received Al 7085-T711

Longitudinal wave speed (C_l)	$6234 \pm 23\,\mathrm{m\,s^{-1}}$
Shear wave speed (C_s)	$3045 \pm 20\,\mathrm{m\,s^{-1}}$
Bulk sound speed (C_0)	$5148 \pm 42\,\mathrm{m\,s^{-1}}$
Density (ρ)	$2935 \pm 3\,\mathrm{kg\,m^3}$
Poisson's ratio (ν)	0.340 ± 0.004
Young's modulus (E)	$73.10 \pm 0.75\,\mathrm{GPa}$
Shear modulus (G)	$27.20 \pm 0.36\,\mathrm{GPa}$

energy is ∼2.5 J. In order to launch a 50 µm thick aluminum flyer, we stretched the pulse duration to ∼21 ns to avoid vibrations in the flyer during flight [**?** **?**]. We also expanded the original ∼13 mm diameter beam to ∼25 mm diameter to protect the lenses in the optical path. We spatially homogenized the stretched and expanded beam using a 50.8 mm diameter diffractive optical element (HOLO/OR) to achieve a top-hat beam profile. Finally, we focused the homogenized beam using a plano-convex lens with 250 mm focal length onto the flyer assembly, resulting in a ∼2.18 mm diameter laser spot. More details regarding the experimental setup of the micro-flyer apparatus can be found in Ref. [**?**].

A schematic of the micro-flyer target assembly is shown in Fig. 1. To make these sample assemblies, we bonded a 50 µm thick aluminum foil onto a 6.4 mm thick borosilicate glass sheet using epoxy. We then used a femtosecond laser to cut 1.5 mm diameter flyer disks from the aluminum foil. Next, we glued a 125 µm thick Kapton spacer with 1.7 mm inner diameter and 3 mm outer diameter onto the flyer disk. We then glued the 3 mm diameter and 200 µm thick sample onto the spacer. We made the inner diameter of the Kapton spacer slightly larger than the flyer diameter, in order to improve the planarity of the flyer during flight.

For a laser-driven microflyer we focus the homogenized laser pulse onto the glass-epoxy interface. Pressure generated by the plasma at the glass-epoxy interface causes the aluminum disk to detach from the glass substrate (generating a flyer) and impact the sample [**?**]. The particle velocity at the rear surface of the sample target is

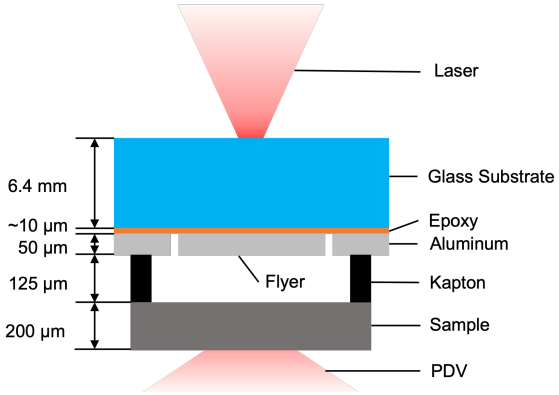

Fig. 1: Schematic of the laser microflyer assembly. Shock is induced in the specimen by an aluminum microflyer disk, which is launched by pressure generated by a plasma at the glass-epoxy interface by the drive laser (top). The rear-surface velocity of the specimen is monitored by photon doppler velocimetry, PDV (bottom).

measured using PDV [**? ? ?**]. More details of the PDV employed in our experiment can be found elsewhere [**? ? ?**]. In this work the 7085-T711 samples were subjected to four nominal impact velocities: 630, 750, 910, and 1140 $\mathrm{m\,s^{-1}}$, so that we could examine a range of spall behavior. The heat-treated samples were subjected to a smaller range of impact velocities in order to focus on comparative mechanisms and to examine incipient spallation.

A schematic of the wave interactions in the spall test is shown in Fig. 2. The micro-flyer plate impacts the target plate specimen at normal incidence (Fig. 2(a)). The impact generates compressive shock waves which propagate from the impact surface towards the free surfaces of both the target and flyer at a shock wave velocity U_S, as shown in the simplified x–t diagram (Fig. 2(b)), sometimes preceded by an elastic precursor propagating at the elastic longitudinal wave speed C_l. The arrival of these waves at the rear surface of the target causes increases in the rear-surface velocity (U_{fs}), as shown schematically in Fig. 2(c); with the elastic precursor arriving at t_1 and the shock wave arriving at t_2. The small kink in the velocity profile between t_1 and t_2 represents the Hugoniot elastic limit (HEL), which indicates the onset of inelastic deformation under these uniaxial strain conditions. The compressive shock waves reflect from the free surfaces as rarefaction fans, which release the compressive

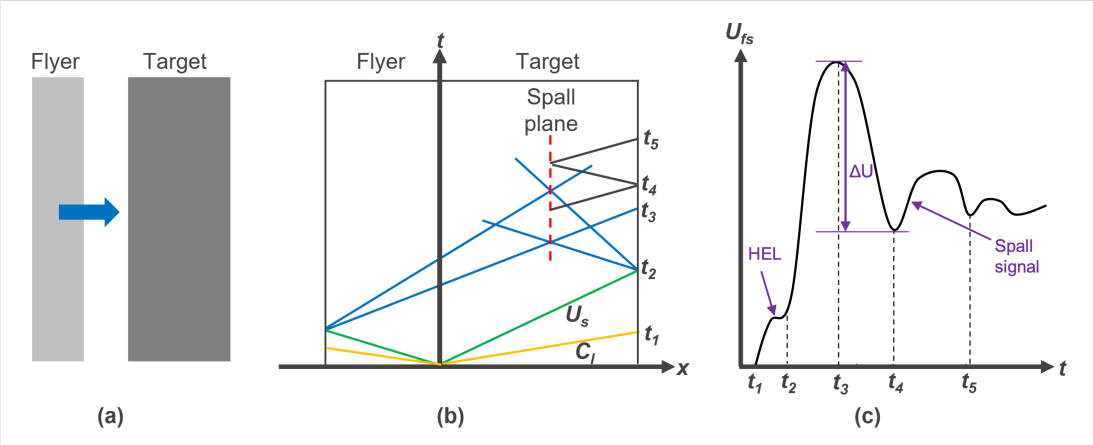

Fig. 2: (a) Schematic of plate impact; (b) x–t diagram (t_1: arrival time of the elastic precursor; t_2: arrival time of the shock wave; t_3: arrival time of the first information of release from the free surface of the flyer; t_4: arrival time of the recompression wave generated by spall failure; t_5: arrival time of the subsequent reflections of wave); (c) free surface velocity profile.

stress over some time. The rarefaction fans from the two free surfaces intersect inside the sample at some time after t_2, creating intense hydrostatic tension. However, the first information of release from the free surface of the flyer arrives at the target rear surface at t_3 (Fig. 2(b)), and U_{fs} begins to decrease at that time. At this time t_3, a region inside the target (denoted by the dashed red line in Fig. 2(b)) is subjected to a rapidly growing nearly hydrostatic tensile stress, and when the tensile stress created there exceeds some critical value, spall failure begins to occur through void nucleation, growth, and coalescence. The voids grow at a large tensile strain rate determined by the effective response of the spalling solid to the local tensile stress state. The formation of these voids creates a failure surface that generates a recompression wave which propagates back towards the rear surface of the target, arriving there at time t_4. The recompressive wave speed ranges from C_0 (the sound speed) to C_l, depending on the rate of the failure process [**?** **?**]. Subsequent reflections of waves bouncing between the target rear surface and the developing spall failure cause oscillations in the free surface velocity after t_4.

The Hugoniot elastic limit (HEL) σ_{HEL} is computed from the measured free surface

velocity history using

$$\sigma_{\mathrm{HEL}} = \frac{1}{2}\rho_0 C_l U_{\mathrm{HEL}}, \tag{1}$$

where ρ_0 is the initial density. The compressive stress associated with the primary shock is given by

$$\sigma_{\mathrm{peak}} = \frac{1}{2}\rho_0 U_S U_{\mathrm{peak}}, \tag{2}$$

where U_S is the shock velocity (in this case estimated from data in Ref. [**?**]), and U_{peak} is the rear surface velocity at t_3 just before release begins. In our experiments, because of the short laser pulse duration and the rise time of the shock, this velocity is typically the peak velocity.

The spall strength is normally defined in terms of the measured pullback velocity (ΔU), defined as the difference between the peak velocity (U_{peak}) at t_3 and the first minimum in velocity at t_4 (Fig. 2(c)) using

$$\sigma_{\mathrm{spall}} = \frac{1}{2}\rho_0 C_0 \Delta U, \tag{3}$$

where ρ_0 is the initial density, and C_0 is the bulk sound speed [**?**]. We estimated the tensile strain rate using

$$\dot{\epsilon} \simeq \frac{1}{2C_0}\frac{\Delta U}{t_4 - t_3}, \tag{4}$$

but we note that various other estimates are used in the literature [**?**]). Note that the conditions of the test are approximately uniaxial strain.

The spall tests were performed along the normal direction (ND) of the rolled material. To prepare specimens for the spall experiments, we cut 3 mm diameter cylinders using wire electro-discharge machining (EDM), with the cylinder axis being the normal direction (ND). Next, we cut 1 mm thick disks from the cylinders (also using EDM) and polished the disks to a thickness of 200 ± 10 µm. Samples for microstructural analysis were prepared by sequential polishing using P1200, P2500, and P4000 SiC sandpaper. Microscopy specimens were etched with Keller's etchant (1% HF, 1.5% HCl, 2.5% HNO_3, balance H_2O) to remove surface oxidation and reveal the microstructure. Samples for electron backscatter diffraction (EBSD) analysis were prepared with the same polishing sequence, followed by polishing with 0.05 µm water-free colloidal silica suspension (Buehler Inc.) and ion milling (with a dual ionized

argon beam at 4.0 kV for 30 minutes at a tilt angle of 4.5° using a Fischione 1060 ion-milling system).

3. Results and discussion

3.1. Microstructure of as-received 7085-T711

In addition to fcc α-Al, x-ray diffraction revealed the presence of three intermetallic phases: Al_7Cu_2Fe, Al_2CuMg (the S phase) and $MgZn_2$ (the η phase) (Fig. 3(a)). There are two types of large precipitates, one which appears bright in the SEM images (Fig. 3(b)) and one which appears dark (Fig. 3(c)). EDS analysis revealed that the bright precipitates are Al_7Cu_2Fe second-phase particles with a typical size of about 1 µm which aggregate into clusters aligned along the rolling direction. The darker precipitates, which are somewhat smaller (200 nm to 400 nm) and more uniformly distributed, have a composition consistent with an Al-Zn-Mg-Cu quaternary phase [**?**]. This phase results from substitution of Al and Cu on the Zn sites in the $MgZn_2$ structure [**?** **?**]. These observations are consistent with prior work on Al-Zn-Mg-Cu alloys [**?** **?** **?** **?**]. We did not pursue characterization of the material to look for smaller (nm-scale) precipitates, because these are believed to be less important than the larger particles for spall void nucleation [**?**]. We note, however, that these small precipitates have a large effect on the dynamic strength of aluminum alloys [**?**] and so will influence void growth (as discussed below).

The aluminum grain structure determined by EBSD is shown in Fig. 4, with an inverse pole figure map, cumulative area-weighted grain size distribution, and pole figure for each of four conditions. Summary statistics regarding the grain size distribution are reported in Table 2. The as-received Al 7085-T711 shows mostly grains that are significantly elongated along the rolling direction, as expected. Annealing at 500 °C results in substantial aluminum grain growth and a broadening of the grain size distribution. (There is also a reduction in the aspect ratio of the grains and some weakening of the crystallographic texture.) SEM and x-ray diffraction analysis (not shown) reveal no significant changes in the distribution or volume fraction of the Al_7Cu_2Fe second-phase particles due to annealing at this temperature.

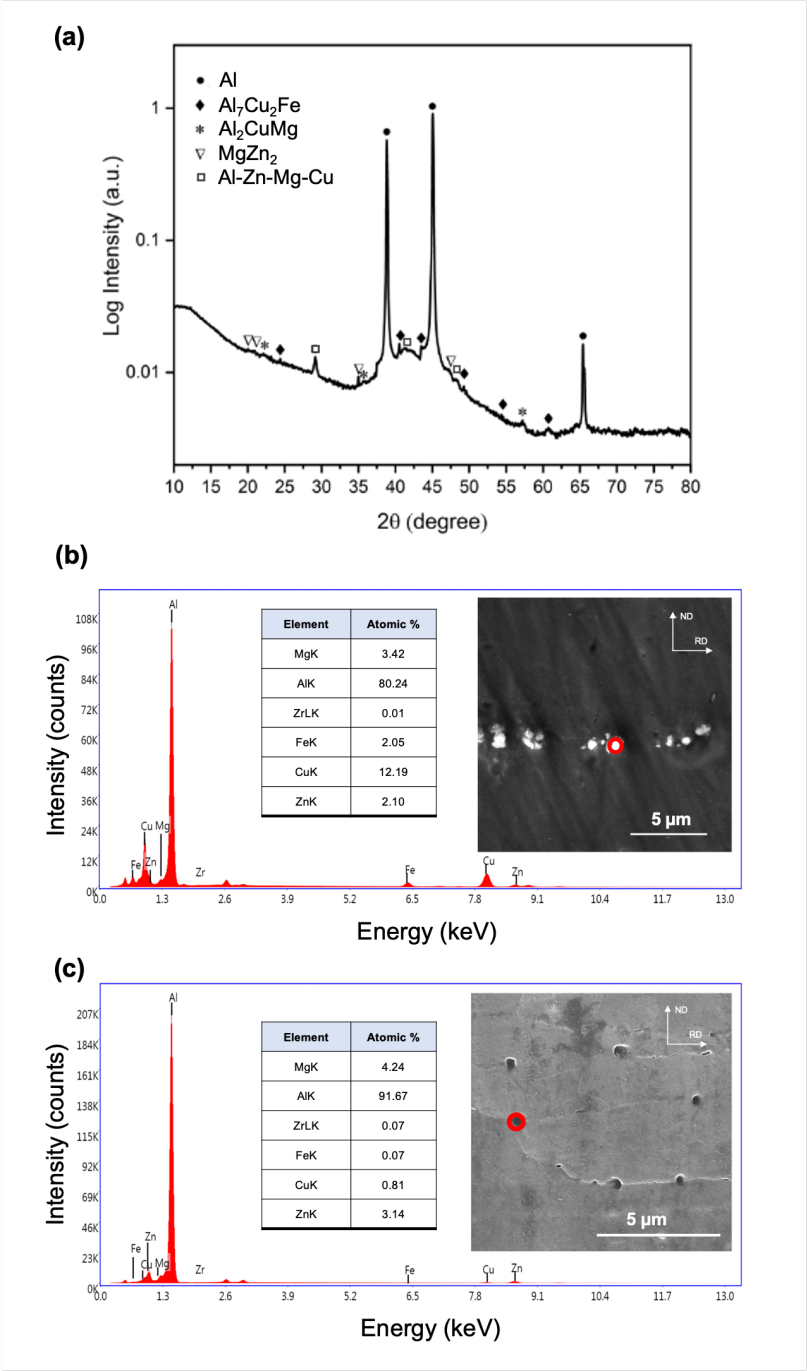

Fig. 3: Second phases of as-received Al 7085-T711. (a) Typical x-ray diffraction pattern. (b) and (c) show scanning-electron microscopy (SEM) and energy-dispersive spectroscopy (EDS) from two kinds of second-phase particles. The bright particles in (b) are Al_7Cu_2Fe and the dark particles in (c) are an AlZnMgCu quaternary phase. In each case the EDS spectrum comes from the region indicated on the SEM image.

Table 2: Effect of annealing at 500 °C on aluminium grain size distribution.

Sample condition	Mean grain area (μm²)	Width of grain area distribution (μm²)	Area-weighted mean grain area (μm²)	Width of area-weighted grain area distribution (μm²)
As-received (T711)	340	780	2120	2250
Annealed 24h	550	1050	2530	2530
Annealed 48h	950	1850	4530	4730
Annealed 192h	2010	3120	6840	5280

Note that the tensile strain rates applied to the microstructures during the spall event are in tension in the ND direction, perpendicular to the primary layering orientation of the grains. Thus the long grain boundaries will be in a strongly tensile loading condition during the development of the spall failure. Note also that the target plate thicknesses in the microflyer spall experiment are 200 μm. This thickness corresponds to a large (but countable, $\sim 7-20$) number of grains across the thickness for each microstructure examined.

3.2. Spall strength of as-received 7085-T711

The as-received Al 7085-T711 specimens were impacted at velocities of 630, 750, 910, and 1140 m s^{-1}, with at least ten samples tested at each impact velocity. (The ability to perform such a large number of spall experiments is one of the great advantages of the microflyer spall approach). Representative free surface velocity profiles are presented in Fig. 5(a) for each impact velocity. The Hugoniot elastic limit (HEL) is clearly discernible, except at the highest impact velocity (1140 m s^{-1}), where it is possibly obscured by our inability to resolve the short interval between the arrival of the elastic wave and the shock wave at the free surface. Based on Equation (1), the measured HEL is 1.51 ± 0.24 GPa. The only comparable HEL data in the literature for a comparable alloy is 1.1 GPa for extruded 7085-T7651 aluminum, and is also from a laser-shock experiment [**?**].

The rear surface velocity histories in Fig. 5(a) show a clear plateau after shock wave arrival only at the lowest impact velocity (630 m s^{-1}), and possibly at 750 m s^{-1}. This plateau is related to the pulse duration, which is approximately twice the flyer thickness divided by the shock wave velocity in the flyer [**?**], or about 10 ns in

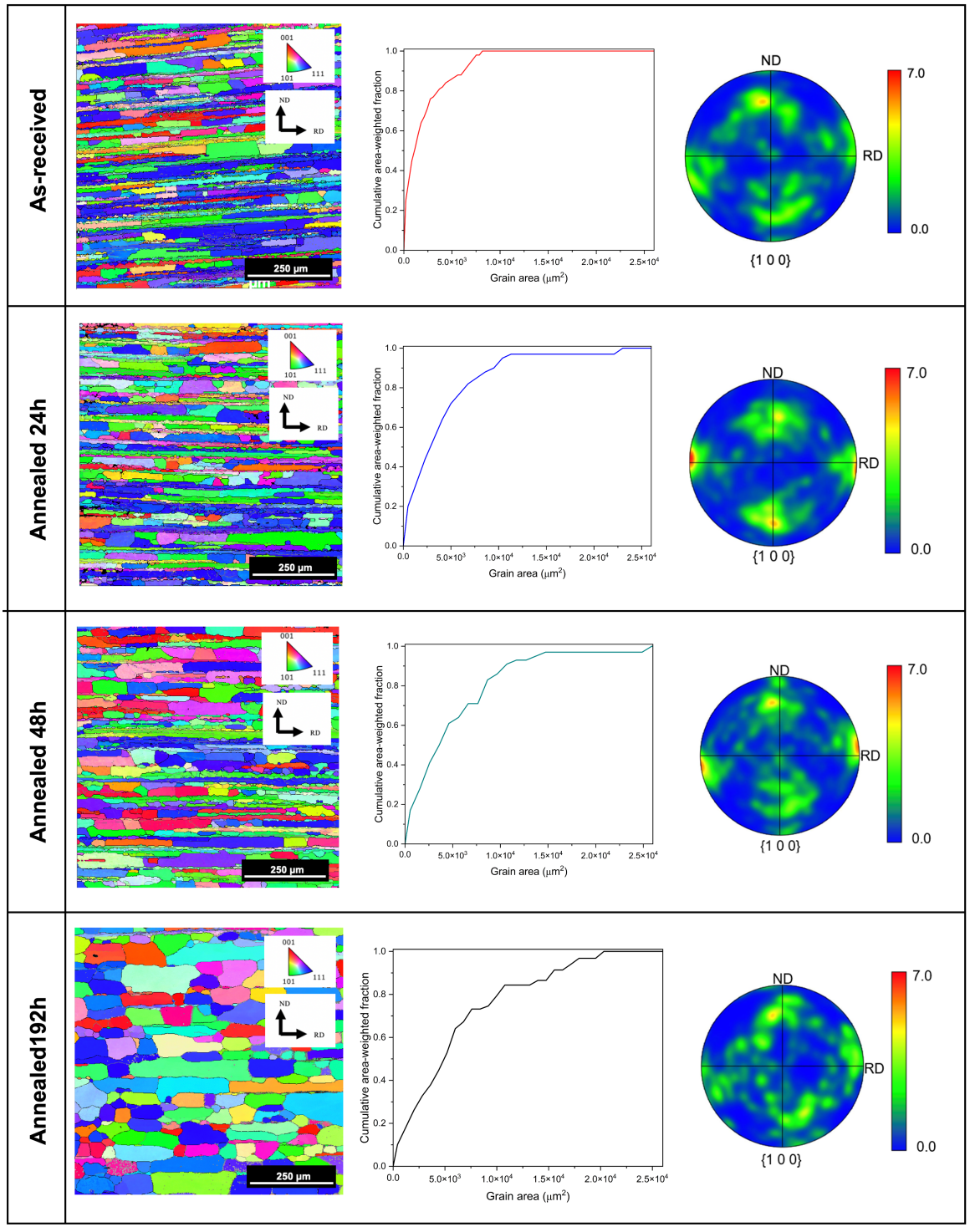

Fig. 4: Microstructure characteristics of Al 7085, including grain structure (EBSD inverse pole figure maps viewed along the transverse direction), left; cumulative area-weighted fraction of grain areas from the EBSD maps, center; and pole figures derived from the EBSD data, right. The top row shows the as-recieved T711 temper, with the other three rows being for material annealed at at 500 °C for 24, 48, and 192 hours. (TD = transverse direction, RD = rolling direction, ND = normal direction)

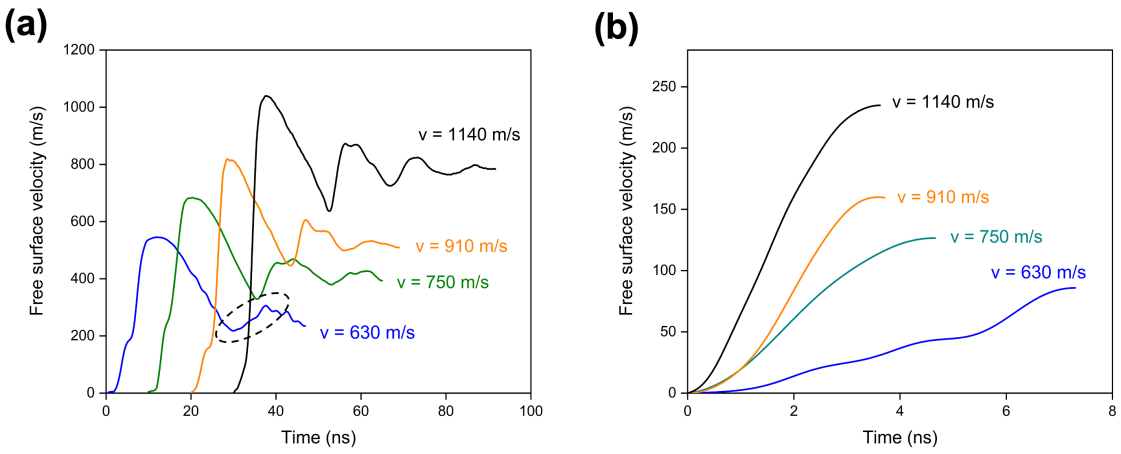

Fig. 5: (a) Free surface velocity profiles for as-received Al 7085-T711 specimens measured at four impact velocities. The time origin of three tests has been shifted slightly for clarity. (b) Evolution of the velocity in the rising part of each velocity profile after the pull-back, all reset to a new baseline corresponding to the bottom of the pull-back signal.

Fig. 5(a). The plateau is less apparent at higher impact velocities because the pulse duration decreases and because our velocimetry processing technique averages velocities over a 3 ns window, smearing narrower plateaus [**?**]. Note that this smearing also affects the observed shock wave rise times.

All four velocity traces in Fig. 5(a) show evidence for spall failure in the form of the pull-back signal, and then show the signature of the recompression wave in the velocity rise after the minimum (e.g., as shown within the dashed ellipse in Fig. 5(a)). The rate of increase of the velocity after the pull-back is related to the rate of growth of the voids (the "damage"). After the pull-back, the rising part in each velocity profile is extracted, normalized in terms of time and velocity, and then plotted in Fig. 5(b). The slope of this signal, which is related to the recompression wave emanating from the spall plane, is seen to increase with impact velocity. Since this slope is correlated with the damage rate, Fig. 5(b) shows that the damage growth rate increases with impact velocity [**? ?**] (i.e., the compressive shock stress before the release begins).

The shock stress, spall strength and strain rate, for each experiment on the as-received material were calculated using Eqns. (2), (3) and (4). The results are plotted in Fig. 6 in terms of the variation of the measured spall strength with applied prior

shock stress (Fig. 6(a)) and with the applied tensile strain rate (Fig. 6(b)). Looking first at the consequences on the prior shock stress, we observe (i) that the spall strength generally increases with the shock stress, and (ii) that the data points from multiple tests at one impact velocity cluster quite tightly, but do have a spread. The latter observation, of the spread in spall strength data at nominally the same impact velocity, is likely a consequence of the inherently stochastic character of the spall process (in terms of availability of nucleation sites) and the relatively small size of our specimens (so that we are effectively sampling the microstructure with each specimen). The former observation, that the spall strength increases with the shock stress, is a common one for aluminum alloys (e.g. the observations on 6061 Al by Chen et al. [**?**]) and relates to the hardening of the material as a result of the shock stress, which makes it more difficult to grow voids (since void growth in metals requires plastic deformation). The consequences of the prior shock on the microstructure have been examined for some aluminum alloys [**?** **?**], and both the saturation of microstructural evolution and thermal softening have been suggested to be important at very high shock stresses.

The observation that spall strength increases with strain rate is consistent with earlier research on aluminum alloys [**?** **?**], but we note here that the range of strain rates that we can achieve in our experiments is quite small, all between 2x10^6 s^{-1} and 4x10^6 s^{-1}. It is likely that we cannot accurately assess the dependence on strain rate with such a small range. The mechanistic reasons for the dependence of spall strength are relatively well understood [**?**] and include the fact that void growth rates are limited by rate effects on the plasticity and the dislocation mobility [**?**].

Our observations on the spall strength of the as-received 7085-T711 alloy are compared with other results in the literature in Fig. 7. Although we could find no data for 7085 Al, there are data available for 7075 Al [**?** **?**] and a Al-Zn-Mg-Cu alloy of similar composition [**?**] that have been obtained at plate impact strain rates ($\sim 10^4$ s^{-1}). The Al-Zn-Mg-Cu alloy from Zhang and coworkers experienced solution treatment at 470 °C, cold water quenching and three different aging conditions: Naturally aged (NA) at room temperature for 30 days, peak aged (PA) at 165 °C

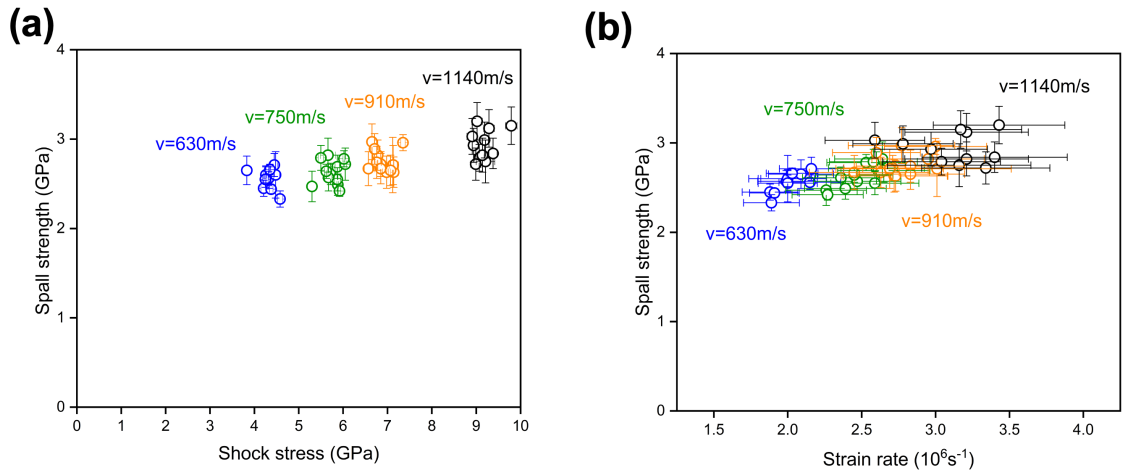

Fig. 6: Spall strength of as-received 7085-T711 in the normal direction plotted against (a) shock stress and (b) tensile strain rate. The spall strength increases with both factors.

for 24 h and over aged (OA) at 120 °C for 24 h. The spall strengths of 7075 Al are typically observed to range from 1.3 GPa to 1.8 GPa at these rates, much lower than the 2.5 GPa to 3.5 GPa that we observe for as-received 7085-T711 at our higher strain rates ($\sim 1 \times 10^6\,\mathrm{s}^{-1}$).

Fig. 8 shows the residual spall damage observed in specimens of the as-received materials shocked at different impact velocities, determined through X-ray computed tomography. The degree of damage increases with increasing impact velocity, consistent with the advancing stages of spall failure, with only a small degree of damage observed in the spall plane at the lowest impact velocity. Complete spall is observed at a velocity of $910\,\mathrm{m\,s}^{-1}$.

3.3. Microscopic character of spall failure in as-received material

The microscopic aspects of spall failure in this material can be assessed by examining SEM images of regions around spall damage initiation sites, taken from specimens that were sectioned after the spall tests, as shown in Fig. 9. In general, grain boundaries, precipitates, and second-phase particles are expected to be potential nucleation sites for microvoids [**?**]. In the as-received 7085-T711 alloy, damage mostly initiates in dense clusters of Al_7Cu_2Fe second-phase particles (Fig. 9(a)) at the lowest impact velocity ($630\,\mathrm{m\,s}^{-1}$), probably due to decohesion between the second phase particles

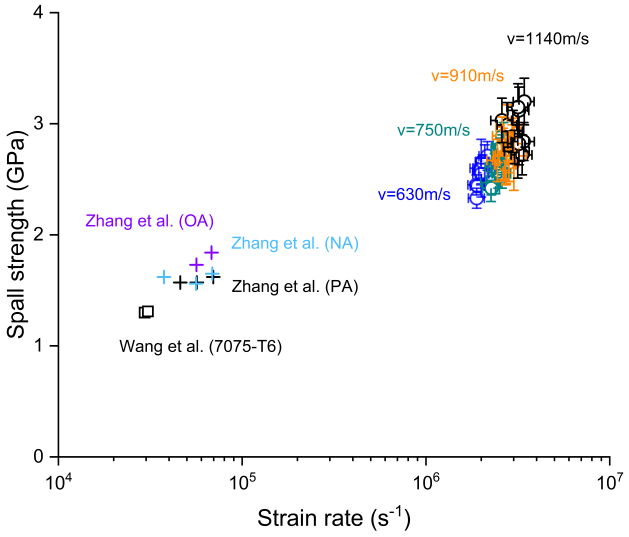

Fig. 7: Measured spall strength as a function of strain rate for as-received 7085-T711 (this work) with prior data from 7075 Al-T6 from Wang and coworkers [**?** **?**] and a Al-Zn-Mg-Cu alloy of similar composition from Zhang and coworkers [**?**]. (PA = peak aged, OA = overaged, NA = naturally aged)

and the base metal [**?**]. On the other hand, spall damage does not appear to develop near AlZnMgCu quaternary second-phase particles at this velocity (Fig. 9(b)). At higher impact velocities damage continues to initiate near Al_7Cu_2Fe clusters, but we also observe damage developing at Al grain boundaries (Fig. 9(c),(d)). This suggests that the grain boundaries are somewhat stronger than the Al_7Cu_2Fe-matrix interfaces, explaining why a higher impact velocity is necessary to nucleate voids there.

3.4. Spall behavior of heat-treated specimens

Our observations on the as-received Al 7085-T711 specimens showed the importance of Al_7Cu_2Fe clusters and aluminum grain boundaries for the initiation of spall damage. To further explore the role of microstructure on the spall strength, we annealed specimens at 500 °C for 24, 48, and 192 h (followed by a water quench) to change the aluminum grain size (Figure 4) and possibly reduce the crystallographic texture [**?** **?**]. These heat-treated specimens were impacted at the lowest impact velocity (630 m s^{-1}) to study incipient spall failure. Interestingly, annealing at this

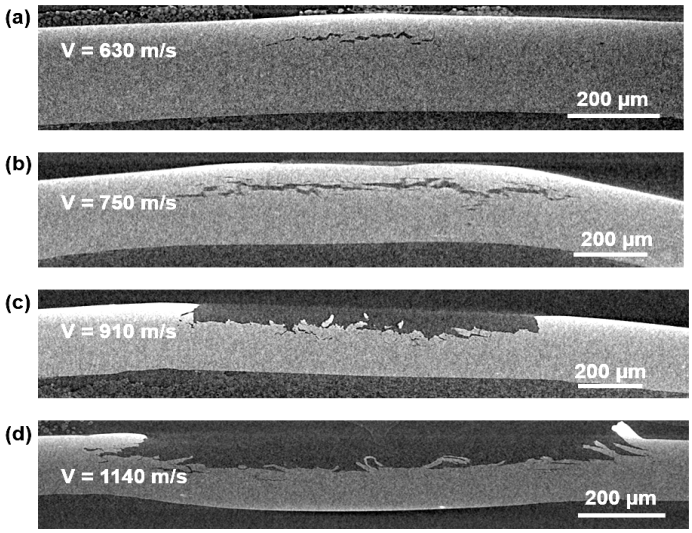

Fig. 8: X-ray computed tomography sections of as-received Al 7085-T711 specimens shocked at (a) $630\,\mathrm{m\,s^{-1}}$ (b) $750\,\mathrm{m\,s^{-1}}$ (c) $910\,\mathrm{m\,s^{-1}}$ and (d) $1140\,\mathrm{m\,s^{-1}}$, which illustrate advancing stages of spall failure. The contrast of the images has been enhanced to maximize the visibility of voids.

temperature has only a minor effect on spall strength, as shown in Fig. 10(a). This is probably because nucleation of spall voids is still associated with clusters of Al_7Cu_2Fe second-phase particles and the size of these particles is not much affected by annealing, as shown in Fig. 11. This indicates that the primary effect of annealing at 500 °C on spall strength is associated with an increase in the average aluminum grain size.

Upon closer examination of the spall strength data in Fig. 10(a), however, it appears that although the average spall strength is increased only slightly by annealing, the scatter in spall strength increases. This is correlated with an increase in the standard deviation of the aluminum grain size measured by EBSD, as shown in Fig. 10(b). This suggests that the scatter in the spall strength measurements may be due to the stochastic effects of microstructural variation on the spall process. This is also an important point of comparison between laser micro-flyer measurements and more traditional gun-type measurements: the loaded volumes of each sample for the micro-flyer measurement ($\sim 10^{-10}\,\mathrm{m^3}$) are much smaller than those of traditional gun-style plate impact spall measurements ($\sim 10^{-7}\,\mathrm{m^3}$). In each case the measurement will be influenced by the inhomogeneous microstructure on the scale of the sample. For traditional techniques these could also reflect relatively large-scale variations (such as

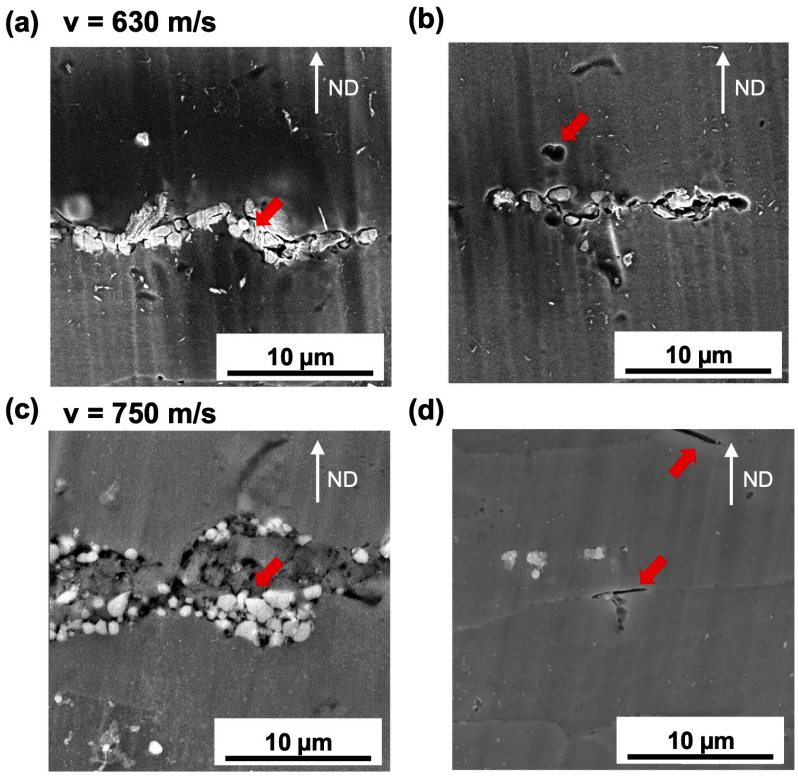

Fig. 9: SEM images near the crack initiated sites of as-received Al 7085-T711 shocked at (a,b) $630\,\mathrm{m\,s^{-1}}$; (c,d) $750\,\mathrm{m\,s^{-1}}$. The contrast of the images is enhanced to maximize the visibility of microstructures.

macrosegregation or forging flow lines, for example), but in the case of the micro-flyer measurement the sample size approaches the scale of the grain structure itself. This provides an interesting opportunity to use the small-scale measurements to directly probe the effect of microstructure variation on spall void nucleation and growth, but also points out that multiple experiments are needed to assess the spall strength.

As noted above, the spall strength of the annealed specimens is slightly higher than that of the as-received Al 7085-T711 specimens (Fig. 10(a)). Quasi-static tensile tests (not shown) indicate that annealing at 500 °C reduces both yield strength and ultimate tensile strength relative to the as-received Al 7085-T711. On the basis of models such as that of Wu and coworkers [**?**] this would suggest that voids should grow more easily, reducing the spall strength. The competing term is of course the ease of void nucleation: If it is more difficult to nucleate voids, the spall

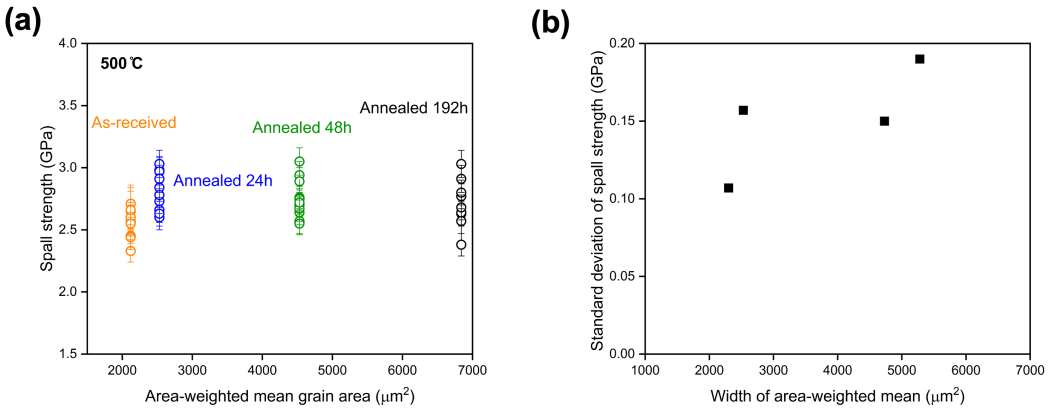

Fig. 10: Effect of annealing at 500 °C, which increases the aluminum grain size. The spall strength increases slightly for the shortest annealing time, but is unchanged for longer times. However, the scatter in spall strength (b) increases with increasing grain size.

strength should increase. Note that the maximum in the tensile stress corresponding to spall occurs at relatively low porosities [**?**], and so void coalescence and associated ductility effects do not control the spall strength. Since our observed spall strengths are slightly higher in the annealed material but the yield strength is lower, we conclude that void nucleation is more difficult in the annealed materials. Given that the two observed void nucleation sites are the Al_7Cu_2Fe second-phase particles (Fig. 11) and the aluminum grain boundaries, but the second phase particles are not significantly affected by annealing, it appears that the change in the grain size (and possibility reduced defects at the grain boundaries) as a result of annealing has reduced the grain boundary contribution to nucleation in the annealed materials. This is also consistent with the EBSD observations that the grain boundary area per unit volume is reduced by annealing (Fig. 4).

To confirm the importance of the of Al_7Cu_2Fe second-phase particles for spall strength, we annealed some specimens at a higher temperature, 600 °C, for 24 h to fully solutionize the material and eliminate the particles (Fig. 12(a)-(c)). Our expectation was that in the absence of these particles, formation of spall voids would require activation of some other type of nucleation site, presumably at a higher stress level. The corresponding histograms of spall strength data are shown in Fig. 13, where we

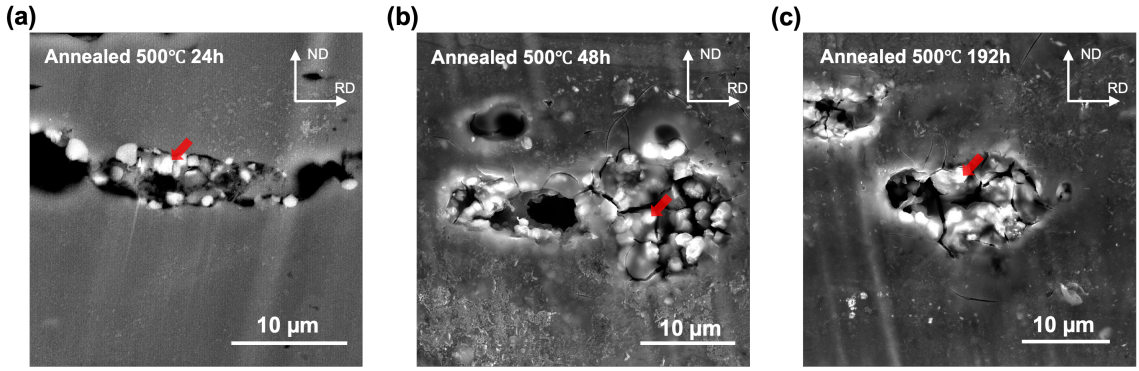

Fig. 11: Spall damage in specimens annealed at 500 °C and tested at an impact velocity of 630 m s^{-1}. Damage is associated with the presence of Al_7Cu_2Fe second-phase particles (bright in the images) in each case. Note by comparison with Fig. 3(b) that the size of the Al_7Cu_2Fe particles is not significantly affected by annealing at this temperature. (The contrast of the images has been enhanced to maximize the visibility of microstructures.)

see that the solutionizing treatment does indeed increase the average spall strength, to 3.2 GPa compared to 2.6 GPa for the as-received Al 7085-T711 material. Although the aluminum grain size also increases due to the heat treatment (Fig. 12(d)), as noted above the average grain size appears to have little effect on spall strength. Therefore, we conclude that this increase is due mostly to the elimination of spall void nucleation sites by elimination of the second-phase particles.

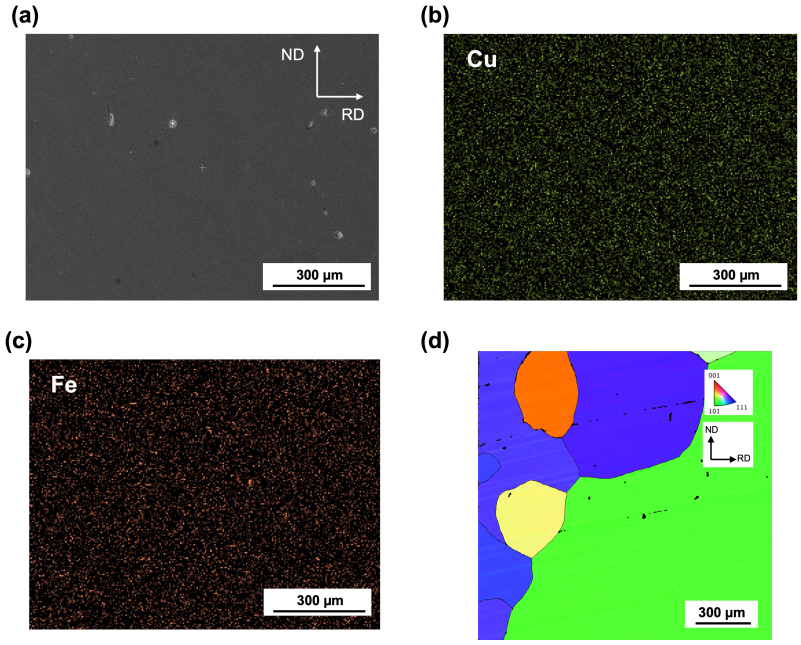

Fig. 12: Microstructure of a specimen solutionized at 600 °C for 24 h. The SEM micrograph in (a) and the Cu (green) and Fe (red) EDS elemental maps in (b) and (c) show that there are no Al_7Cu_2Fe second-phase particles. Part (d) shows the grain structure (EBSD inverse pole figure) viewed along transverse direction (TD).

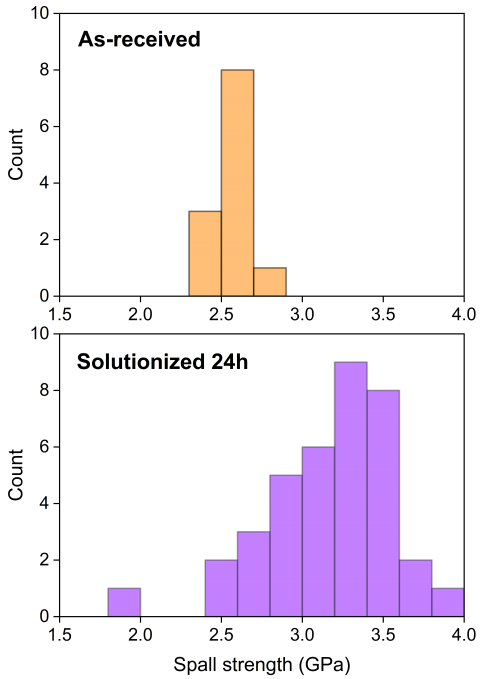

Fig. 13: Effect of annealing at 600 °C for 24 h on spall strength. The histogram in the spall strength increases for the annealed specimens as compared with the as-received Al 7085-T711 specimens.

4. Conclusion

We have applied a laser-driven micro-flyer technique to study the spall response of Al 7085-T711, and find that spall strength increases with shock stress as well as with increasing strain rate. Spall voids nucleate primarily at second-phase Al_7Cu_2Fe second-phase particles at low impact velocities, and also at aluminum grain boundaries at higher impact velocities. Heat-treatment of the material to increase the aluminum grain size raises the spall strength only modestly, but does increase the variance in the spall strength measurement, presumably because the small probed region in the micro-flyer technique makes it more sensitive to microstructure variations. Finally, annealing at a temperature high enough to solutionize the material and thus eliminate the Al_7Cu_2Fe second-phase particles results in a substantial increase in spall strength. Taken together, our observations clearly indicate that incipient spall strength is dominated by the presence of large (micron-scale) second-phase particles that act as nucleation sites for spall voids, with the aluminum grain size playing a secondary role.

CRediT authorship contribution statement

Dung-Yi Wu: Conceptualization, Methodology, Investigation, Writing – original draft, Software, Formal analysis. **Chengyun Miao**: Conceptualization, Methodology, Investigation, Writing – original draft, Software, Formal analysis. **Christopher DiMarco**: Methodology, Software, Formal analysis, Validation. **Debjoy D. Mallick**: Methodology, Validation. **K.T. Ramesh**: Methodology, Writing – Review and editing, Supervision, Funding acquisition. **Todd C. Hufnagel**: Conceptualization, Methodology, Writing - Review and editing, Supervision, Funding acquisition, Project administration.

Declaration of competing interest

The authors declare that they have no known competing financial interests or personal relationships that could have appeared to influence the work reported in this paper.

Data availability

Data will be made available on request to the corresponding author.

Acknowledgements

We gratefully acknowledge Tyrel McQueen and Johndavid Sabedra for assistance with the x-ray diffraction measurements, Jim Spicer for assistance with the ultrasonic elastic wave measurements, and Hao Sheng for assistance with flyer preparation. This material is based upon work supported by the National Science Foundation under Grant No. 1921959. Portions of this work were performed at the Hopkins Extreme Materials Institution (HEMI) and at the Materials Characterization and Processing (MCP) center in the Whiting School of Engineering at Johns Hopkins University.